IEEE Access
Multidisciplinary | Rapid Review | Open Access Journal

Received 24 November 2024, accepted 9 December 2024, date of publication 13 December 2024,
date of current version 23 December 2024.

Digital Object Identifier 10.1109/ACCESS.2024.3517543

RESEARCH ARTICLE

Automatic Characterization of High-Performance MEMS-Based IR Sensors

MATTHEW BENSON, RYAN W. PARKER, MELISA EKIN GÜLSEREN, (Member, IEEE), AND JUAN SEBASTIÁN GÓMEZ-DÍAZ, (Senior Member, IEEE)
Department of Electrical and Computer Engineering, University of California at Davis, Davis, CA 95616, USA

Corresponding author: Juan Sebastián Gómez-Díaz (jsgomez@ucdavis.edu)

This work was supported in part by the U.S. Department of Defense—Army under Grant W911NF2210067, in part by the National Institutes of Health under Award R01CA273253, and in part by NSF under Grant EECS 2314932.

ABSTRACT The next generation of infrared (IR) sensors may enable unprecedented applications in fields like spectroscopy, health monitoring, and communication systems. For instance, metasurface-enhanced micro-electromechanical system (MEMS)-based IR sensors have demonstrated excellent performance in terms of responsivity and spectral-selectivity. However, it is burdensome to experimentally determine the performance limits of this and other IR sensing technologies as it requires time-consuming and expensive systematic testing not always feasible in research settings. To address this challenge, an automated solution for characterizing miniaturized sensing devices is presented in this paper and applied to experimentally determine the performance limits of MEMS-based IR sensors. The system offers low-cost, rapid, and automated characterization of on-chip IR sensors, determining key performance metrics such as noise, responsivity, and noise-equivalent power. The platform is flexible, easily adapted to different types of devices, chip layouts, and light sources, and is designed to test a large number of sensors within the same wafer —spending $\sim$ 20 seconds per device— using a combination of optical and radiofrequency interrogation techniques. The system has been applied to test over 1500 MEMS-based IR sensors. Collected data revealed hidden trade-offs between responsivity and noise with respect to the device thickness and allowed a statistical analysis of sensing response versus device geometrical dimensions. The best-performing devices exhibit a quality factor, responsivity, fluctuation induced noise, and noise-equivalent power of 2391, 164 Hz/nW, 0.257 Hz/$\sqrt{\text{Hz}}$, and 5.01 pW/$\sqrt{\text{Hz}}$ respectively. The proposed automated platform provides an efficient and cost-effective solution for characterizing the next generation of IR sensing devices.

INDEX TERMS Automation, characterization, infrared, micro-electromechanical systems (MEMS), metasurfaces, radiofrequency (RF), sensors.

I. INTRODUCTION

Infrared (IR) sensors play a critical role in many systems vital to our lives [1], [2], [3], [4], [5], from medical devices to national defense. Before the advent of narrowband semiconductor alloys such as the widely used II–VI ($Hg_{1-x}Cd_xTe$), the first IR detectors were built on polycrystalline lead salt. Since then, the development of photo-lithography and advanced nano-machining has greatly expanded the different types of IR detectors available, ranging from thermopiles, bolometers, pyroelectric detectors, and photodetectors to exotic configurations like cantilevers and golay cells [6], [7]. More recently, radiofrequency (RF) micro-electromechanical systems (MEMS) loaded with ultratin metasurfaces have lead to a new type of IR sensors exhibiting high performance at room temperature [8], [9], [10], [11]. IR sensing technology has quickly become a large and diverse field, yet testing IR sensing devices faces a significant bottleneck due to traditionally slow development methods [12], [13]. For instance, the characterization of just a single device usually requires time consuming processes such as dicing and wire-bonding that hinder the overall testing throughput. While companies mass-producing semiconductor chips have advanced micro-probe stations that can automate

The associate editor coordinating the review of this manuscript and approving it for publication was Yogendra Kumar Prajapati.

the measurement of thousands of dies, this technology is only cost effective when manufacturing on an industrial scale and it does not provide the capabilities required to explore novel IR sensors. Testing challenges are even more evident in the context of RF-MEMS spectrally-selective IR sensors [8], [9], [10], [11] as these are complex devices whose response is determined by multiple parameters, including advanced resonators designs, geometrical dimensions, and material properties and thicknesses, among others. For instance, most works usually report the metrics of just one specific RF-MEMS IR device that may exhibit suboptimal performance and might not capture the full potential of this technology. The ability to characterize hundreds or thousands of IR sensors would open new venues to explore the fundamental limits of this and other sensing platforms and to determine quasi-optimal device configurations. Thus, there is a clear need for flexible and affordable automated testing systems capable of accommodating DC, RF, and IR interrogation techniques without compromising testing throughput and price.

State of the art high-throughput testing systems for IR sensors do not usually allow for RF excitation and processing that emerging sensing technology requires, or are unable to provide wide-spectrum IR characterization. For instance, some measurement systems have been developed for silicon photonics [14], [15], but they have not incorporated high testing throughput. Furthermore, they are restricted to operate with devices that use clamped optical fibers. Similarly, a promising system is focused on RF/DC testing [16], but it relies on fiber waveguides that may not be suitable for general IR sensors. Preliminary steps to develop systems combining both RF and IR signals have lead to powerful cryogenic testing platforms [17] that still lack the throughput that automation can achieve. While automated sample positioning has been demonstrated in some systems [18], they do not allow for simultaneous RF and IR testing. Along this line, the testing of complex visible light MEMS devices was performed in the development of the digital micro-mirror devices (DMD) [19]. These complex optical MEMS devices required a unique testing procedure that includes complementary metal-oxide semiconductor (CMOS), MEMS, and optical characterizations. While the process was completed with automated robotic control of their testing equipment, the characterization was conducted only over a small sample of devices.

In this work, we present a cost-effective system that enables the automated characterization of on-chip IR sensor devices (Fig. 1) and apply it to explore the performance limits of MEMS-based IR sensors. Compared to bulky and expensive industrial characterization equipment, this system only requires a 3D printer, inexpensive stepper motors, and a microcontroller in combination with equipment usually already available in a research laboratory. The goal of this platform is to provide researchers the ability to quickly characterize a large number of devices in terms of RF response, quality factor, fluctuation induced noise, IR responsivity, and noise equivalent power (NEP), among other metrics. The system implements highly flexible testing methods that can be adapted to a wide variety of device geometries, chip layouts, and sensing technologies. Analysis of the data produced by the system yields wafermaps, device trends, and statistics that can be analyzed along with design parameters, thus enabling a better understanding of the devices under test and easily determining optimal geometrical dimensions. To illustrate the operation and utility of the proposed platform, 1512 IR sensors based on RF-MEMS devices loaded with ultrathin metasurfaces are characterized. These devices are based on aluminum nitride (AlN) resonators with 1 μm and 500 nm thickness. Results comprise a large number of metrics versus geometrical parameters that provide valuable physical insight into the device response and allows the user to identify optimal parameters. A subset of the collected data for the 1 μm-thick devices was reported in Ref. [8], a work that focuses on the fundamental limits on this sensing technology but does not describe how to collect large amount of sensing metrics in an automatized manner. Our study experimentally shows that both the IR responsivity and the fluctuation induced noise decreases as the device thickness increase. These two metrics tend to balance, and thus IR sensors with a NEP in the ~ 20 pW/$\sqrt{\text{Hz}}$ range can be obtained in optimal devices with different thickness. Moving beyond, the proposed platform can be applied to test a wide variety of on-chip IR sensors, including emerging RF-MEMS technologies with state of the art performance [8], [9], [10], [11] as well as devices with standard DC readout, such pyroelectric [20] and bolometer [21] sensors and photodetectors [6].

The rest of this paper is organized as follows. Section II describes the proposed measurement system. Section III briefly overviews the IR sensors under test. The relevant metrics required to characterize RF-based IR sensors are provided in Section IV, together with the approach to determine them in practice. Section V outlines the operational procedure to characterize a large number of devices. Section VI discusses the measured results and provides an statistical overview of the sensors performance. Finally, Section VII concludes this paper.

II. SYSTEM DESCRIPTION

The proposed IR characterization system is illustrated in Fig. 1. It is composed of a precision motorized XY translation stage that holds the chip under test, a motorized micro-probe arm, a blackbody radiator, and a linear stage holding the infrared optics. On the XY translation stage, a 3D printed vacuum chuck is employed to securely hold the chip in place. The optical components can be moved in or out of the beam path by the linear stage, allowing control over the incident IR radiation on the device at the micro-probe tip. The platform is designed to automatically land a ground signal ground (GSG) RF microprobe on each of the devices within the chip. After landing, each device undergoes RF and IR characterization. The probe is then lifted and landed on the

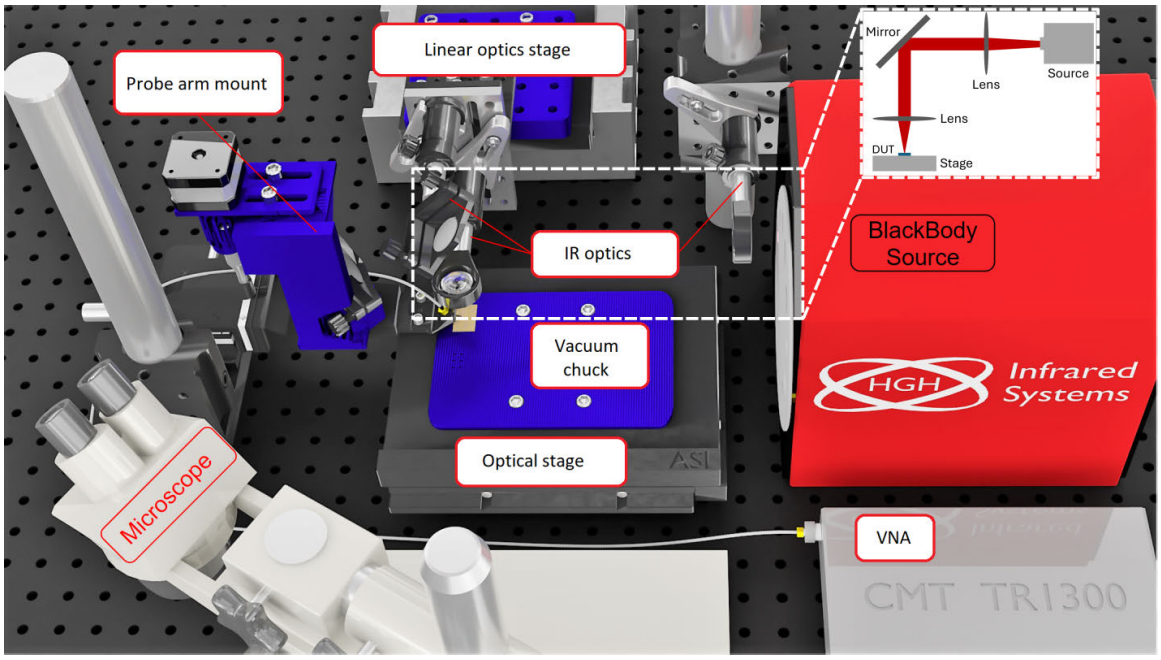

FIGURE 1. The proposed IR characterization system comprises a high precision XY stage, a micro-probe arm with a 3D printed motor mount, a vector network analyzer, a blackbody radiator, and an optics assembly on a linear stage. The linear optics stage holds the optical path to focus IR radiation onto the sample at the micro-probe tip. A 3D printed vacuum chuck is bolted to the stage to secure the chip under test. The vector network analyzer connects to the micro-probe arm for RF characterization. The microscope is used to align the chip and perform the initial probe landing onto the chip under test. The top-right inset illustrates the IR beam path.

next device. This process is repeated until all devices on the chip are characterized. In the following, an overview of the different parts that compose the system is presented.

A. 2D OPTICAL STAGE

The stage that moves the sample is a precise ASI MS-2000 stage that has positional repeatability less than 1 μm, and features closed-loop feedback for precise positioning and a serial interface for remote automation. The stage has been coupled onto a 3D printed part to allow direct mounting on an optical table. The stage has a maximum movement of 12 cm by 11 cm, which sets the maximum sample size the system can accommodate.

B. VACUUM CHUCK

A dedicated vacuum chuck was designed, 3D printed, and secured to the optical stage (Fig. 2). The chuck provides a flat surface with small holes that adheres the chip securely when low vacuum is applied. A vacuum chuck is necessary to keep the chip stationary on the stage during probing. Specifically, the vacuum chuck comprises two 3D-printed plates that bolt together sandwiching the top layer of the ASI stage. The top plate features a grid of small holes connected to a network of small tunnels inside the vacuum chuck, each with a diameter of 3 mm. These tunnels lead to a small outlet port on the back of the vacuum chuck. At the outlet port, a small vacuum pump provides the suction necessary to secure the chip to the chuck for probing. Two sample locations are available, one for a chip and one for a calibration substrate. By connecting

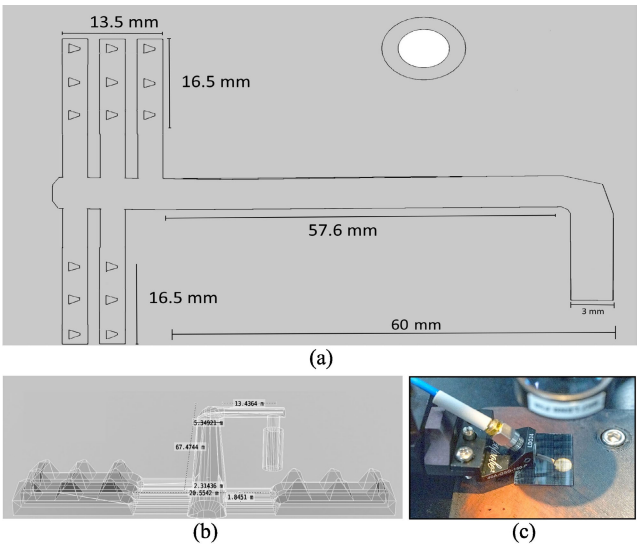

FIGURE 2. Vacuum chuck designed to secure the chip to the optical stage of the platform. (a) Top-down view of the holes and the tunnel system that provides suction to the bottom of the chip. Two different mounting points are supplied for sample and calibration substrate. (b) 3D rendering of the tunnel system and its corresponding dimensions. (c) Picture of the 3D-printed physical chuck. The print material is ABS mixed with 15% chopped carbon fiber. The orange color is a rubber sealant that has been polished into the surface.

the vacuum pump to this outlet port, the negative pressure required to secure the chips to the stage is provided.

While commercial vacuum chucks employed in probe stations are robust, they are usually also large, bulky, heavy,

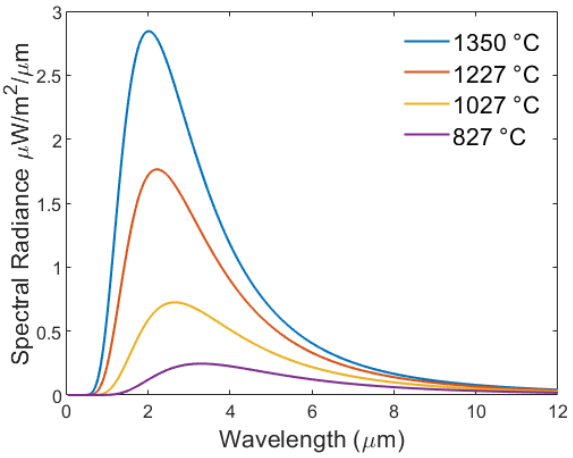

FIGURE 3. Spectral profile of a blackbody radiator irradiance for different temperatures.

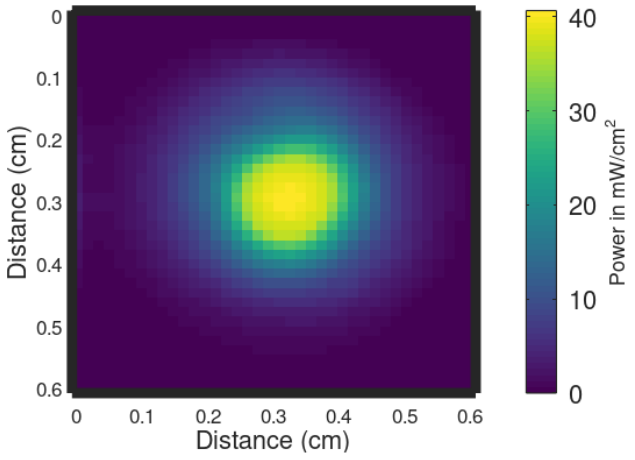

FIGURE 4. Measured spatial power density of the IR beam impinging onto the chip holder of the system. The IR source is an HGH model CRN1350, collimated and focused with wideband IR lenses and measured by scanning a Thorlabs PDAVJ10 IR detector with the precision ASI stage.

and lack flexibility to be customized in dedicated testing systems. One important aspect of the chuck is that it should exhibit an exceptionally smooth and flat surface. This was achieved by printing polylactic acid (PLA) filament on a flat glass bed [22]. When using this approach, the bottom layer, i.e., the chuck surface, melts against the glass, filling in any cracks left from the lines of plastic extrusion. Without a glass bed, the ridges on the surface will cause air leakage and poor vacuum adhesion. Alternatively, polishing the surface with sealant can allow the use of strong filaments such as carbon-fiber ABS or nylon can be used. The polishing is necessary for these higher temperature filaments because the filament extrusions leave gaps in the surface that do not melt together.

C. BLACKBODY RADIATOR AND IR OPTICS

The proposed system employs a HGH CRN1350 blackbody radiator as an IR source. It should be noted that other IR sources, including optical parametric oscillators (OPO) [23] and quantum cascade lasers (QCLs) [24], can be adapted to work within this system. QCLs generate coherent IR light around a given wavelength and therefore multiple QCLs are required to cover a relatively broad IR spectrum region. OPO lasers generate coherent IR light with a narrow linewidth and are tunable over a broadband spectral region. The main advantages of using an OPO or an array of QCLs include (i) the ability to individually test the DUT response at desired wavelengths; and (ii) perform power-controlled experiments. The main disadvantages are price - as both QCLs and OPO are significantly less affordable that thermal emitters - and ease of use. The blackbody radiator employed in our system is capable of heating up to 1350° C, and possesses an emissivity greater than 99% after calibration, a temperature stability of 0.1 °C, and an accuracy of less than 2° C [25]. Fig. 3 shows the spectral irradiance of the blackbody radiator at different temperatures, following Planck's blackbody law. The spatial profile and power level of the IR beam impinging on the 2D stage has been characterized in Fig. 4. To this purpose, a mercury-cadmium-telluride sensor (Thorlabs PDAVJ10 [26]) has been located on the ASI XY translation stage and employed to raster an image of the focused spatial IR radiation using a lock-in amplifier [27] and a chopper. The PDAVJ10 sensor has an active area of 1 mm by 1 mm, which limits the spatial resolution of the image. Since the sensor is placed in the same location the chip is tested, this radiation profile is used to determine the power that is reaching the device under test and to account for the spectral transmission/reflection of all IR components employed in the system.

Aiming to control the illumination of the device under test, a linear stage (Anorad model 91842) is used to move ($\sim$ 9 seconds) IR components in and out from the optical path with micrometer precision. The stage, as illustrated in Fig. 5, hosts two optical components mounted at a 90° angle such that the post assemblies are horizontal. A total of three optics is used to direct the blackbody radiation towards the chip. First, a barium fluoride (BaF_2) lens [28] collimates the output IR light. The collimated beam then arrives at the linear stage and is directed downwards towards the chip by a gold mirror [29]. The beam is then focused onto the micro-probe tip by another BaF_2 lens. A schematic of the IR beam is shown in the inset of Fig. 1. Since the IR light is focused to the plane of the micro-probe tip, it remains focused when the micro-probe lands on a new device.

D. MICRO-PROBE ARM

Aiming to test RF MEMS-based IR sensors, a standard 150 μm GSG 40A micro-probe [30] is used to make electrical connection with the devices. The micro-probe arm is equipped with a motor for driving the micro-probe landing. Electrical testing is performed with a VNA connected to the micro-probe. In case that other type of IR sensors are under test, DC or high-frequency probes can be easily employed in this set-up.

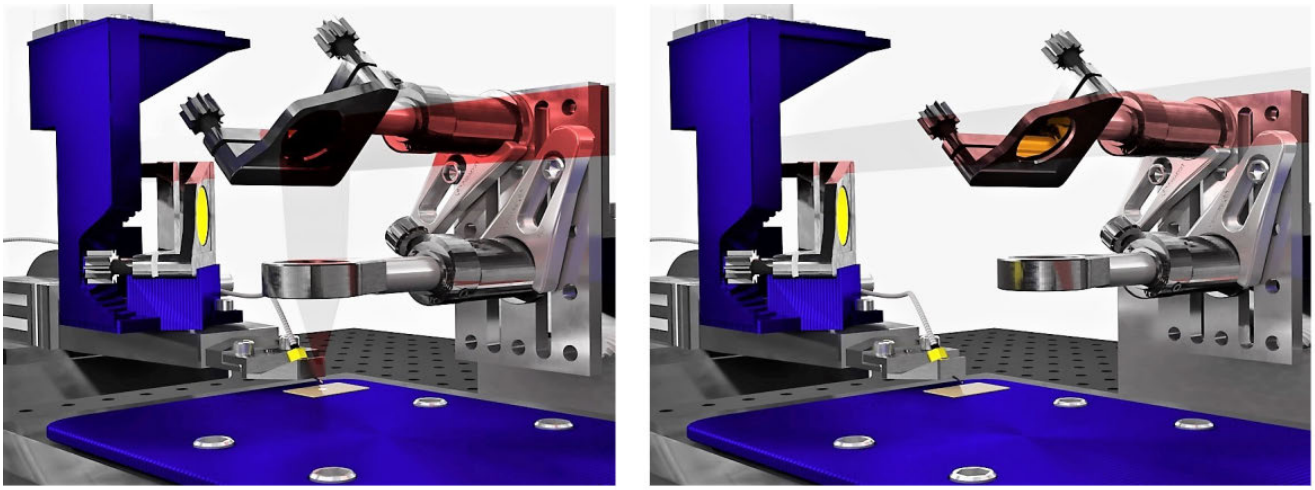

FIGURE 5. Illustration of the automated micro-probe station with IR optical components inserted (a) and retracted (b) from the optical path using a motorized linear stage.

To automate the micro-probe arm, 3D printed parts were designed to couple a stepper motor to the Z-axis adjustment knob of the micro-probe arm, as illustrated in Fig. 6. Specifically, a vertical mount bolts directly to the arm of the micro-probe, and a motor mount holds a NEMA 17 stepper motor and has a notch that slides in a groove on the top of the vertical mount. This allows for fine positioning and to make sure the axes are lined up. Additionally, a motor coupler brings together the motor and the micro-probe Z-axis adjustment arm. The shaft of the motor fits snug inside the printed part, and a screw is used to tighten against the motor shaft and prevent any slip. For the micro-probe arm, a layer of electrical or masking tape is used to ensure a snug fit. Note that the micro-probe arm and motor mount move while the adjustment knob stays in the same position, as it is necessary for the motor mount to have some vertical slack to move independently from the knob.

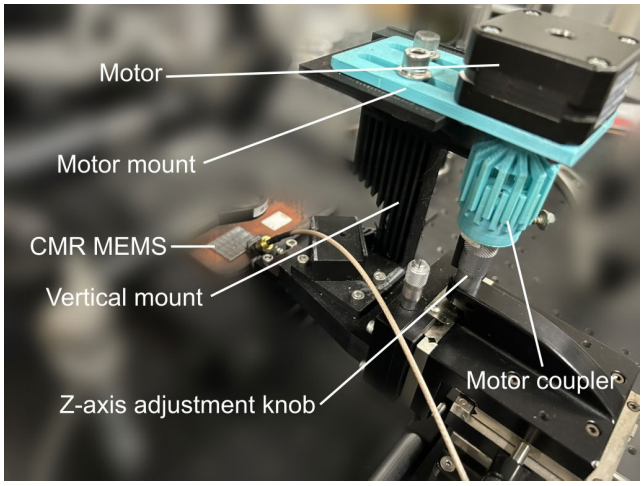

FIGURE 6. Picture of the automated micro-probe arm.

E. ELECTRO-MECHANICAL CONTROL

A microcontroller controls both the linear stage and the micro-probe arm stepper motors using a stepper controller Arduino library called SpeedyStepper [31]. Using this library allows for precise control of the acceleration and position of both stepper motors. The maximum speed of stepper motor operation is highly dependent on the clock frequency of the microcontroller for this library. The Teensy 4.0 [32] employed in this system has a clock speed of 600 MHz and executes two instructions per cycle about 40% of the time based on profiled Arduino code. This leads to stage movement cycles of just 15 seconds. It should be noted that employing a generic Arduino microcontroller [33] to operate the linear stage would have resulted in linear stage movement cycles of over 2 minutes. The system uses a Texas Instruments DRV8825 stepper controller [34] for the micro-probe arm motor, and an Anorad controller for precise and fast control of the linear stage. The electrical connections for the microcontroller and the motor controllers are shown in Fig. 7.

The Teensy 4.0 interfaces with both motor controllers as well as a personal computer via a virtual serial port over USB. Another serial connection is established between the computer and the ASI XY translation stage to send movement commands and receive position data. The devices can be arranged in an array with constant offsets to simplify the measurement algorithm. The entire system is controlled by a home-made MATLAB program, which coordinates and synchronizes the optical stage, linear stage, and the motorized micro-probe arm. Prior to testing, the exact location of the devices within the chip must be loaded into the home-made MATLAB software.

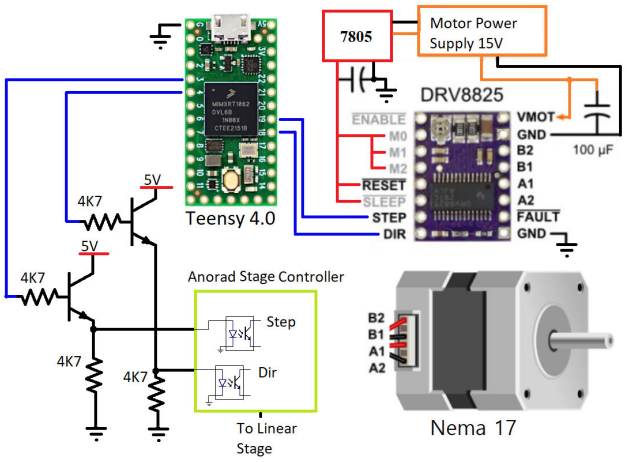

FIGURE 7. Schematic of the electrical connections that govern the proposed platform. A Teensy microcontroller controls two motor controllers, one for the Anorad linear stage and another one (Texas Instruments DRV8825) for the stepper motor NEMA 17.

To interface with the MATLAB program that runs the system, a simple serial interface protocol was devised for the microcontrollers. The automation code and a microcontroller unit (MCU) firmware incorporates redundancy to ensure that the system knows when the micro-probe or stage has completed its movement. For both linear stage and micro-probe move commands, only 1 byte of data is sent to the MCU at a time. Upon receiving the data, the MCU performs the associated action and sends an acknowledgement byte in response. The main software waits to receiving the acknowledgement command before continuing to the next step. This approach prevents that the probe and the stage move simultaneously, keeping the micro-probe from being damaged.

F. RF CHARACTERIZATION

The RF characterization of each device is performed automatically with a Copper Mountain Technologies TR1300/1 vector network analyzer (VNA) [35]. A loopback TCP/IP interface on the host computer created by the VNA software is used to transfer commands and data from a MATLAB program and the hardware. The MATLAB program interfaces with the VNA software which allows sending commands and receiving of data to and from the VNA via USB. Before testing, the VNA is calibrated on the bandwidth where responses are expected. The goal of the VNA in this system is twofold. On one hand, it can measure the scattering parameters of the device under test and monitor their variation versus incoming IR radiation, thus determining the sensor responsivity. On the other, it can operate as an RF source to excite the device under test at a desired frequency and then track the signal variations versus time, which is helpful to determine the sensor fluctuation induced noise.

III. METASURFACE-MEMS RESONATOR

To demonstrate the performance of the proposed IR sensing characterization system, state-of-the-art AlN contour mode

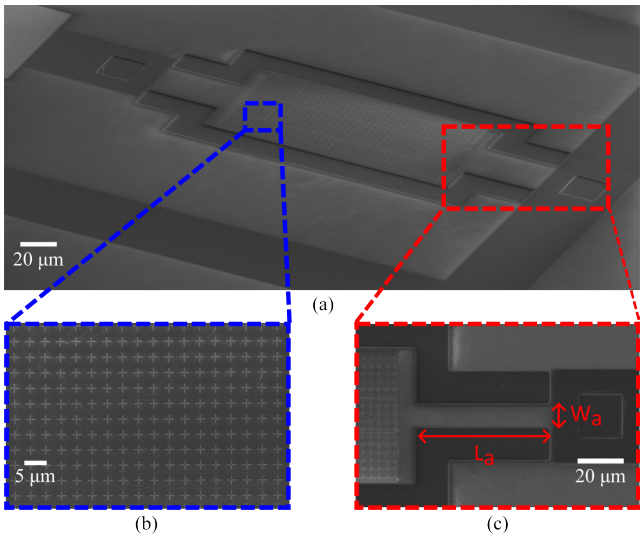

FIGURE 8. (a) SEM image of a CMR MEMS IR sensor. (b) SEM image of the metasurface decorating the resonator body. (c) SEM image of the resonator anchors showing its width W_a and length L_a.

resonator (CMR) RF-MEMS loaded with spectrally selective IR metasurfaces [8], [9], [10] will be tested. A scanning electron microscope (SEM) image of a specific sensor is shown in Fig. 8. These devices exhibit a very high quality-factor at megahertz (MHz) frequencies and become thermal IR sensors by detecting subtle temperature variations in the bulk of the resonator. The resonator itself floats micrometers above the substrate, suspended by two anchors. The metasurface decorating the resonators are made of arrays of crosses or patches that are designed to absorb radiation within a narrow IR band [36], [37], [38], [39], [40], [41], leading to device heating. The heating of the bulk of the resonator causes a shift in the resonant frequency of the device due to the temperature dependent stiffness of the aluminum nitride. Thus, IR radiation can be detected by tracking the frequency shift induced in MEMS RF resonance frequency.

In the following sections, two chips (2.2 cm by 2.7 cm) each containing 756 CMR MEMS resonators are considered. Both chips are identical except for the following difference, one chip contains devices with a 1 μm thick AlN layer and the other contains devices with a 500 nm thick AlN layer. Each chip has a 7 $\times$ 3 array of tiles, with each tile containing a 6 $\times$ 6 array (36 total) of devices (Fig. 9). Devices between tiles are identical, except each tile has a distinct metasurface design, therefore identical devices between tiles target different wavelengths in the mid-IR spectrum. The tiles as well as the rows within each tile are spaced consistently, however, the column spacing within each tile is dependent on device size and is non-uniform.

The CMR MEMS considered resonate around 200 MHz for the 1 μm chip and 175 MHz for the 500 nm chip with device sizes of 60 μm by 125 μm. Each device has the same design, except each row/column contains a different anchor dimension. The anchor width varies from 5 μm to 30 μm in

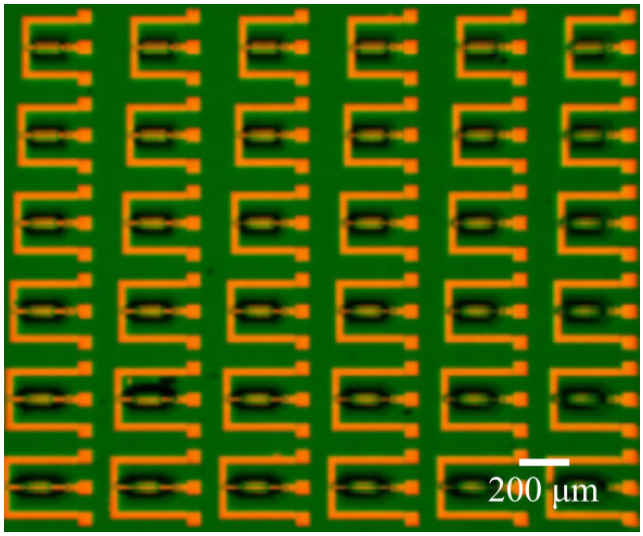

FIGURE 9. Microscope image of the device layout within a single tile. The tiling is repeated on the chip 21 times in a 7 × 3 grid. Each tile has a unique metasurface patterned on all devices in the tile.

increments of 5 μm across the columns. The anchor length varies from 12 μm to 62 μm in increments of 10 μm across the rows. There is a total of 21 different metasurface designs on each chip, 1 design per tile. Each row contains a different geometry, whereas each column contains small geometrical variations to optimize the center wavelength and absorbance. Therefore, there are 7 unique geometries, with each geometry having 3 small variations, leading to 21 total designs. Of the 7 main designs, 5 are based on cross-shaped structures and 2 are based on square patches. The main parameters changed between designs were the lengths/widths of the cross/patch, and the spacing between adjacent crosses/patches. These changes alter the center wavelength and bandwidth of the absorption profile.

It should be noted that the fabrication [8] had a relatively low yield, notably for the 500 nm thick devices. While a total of 1512 (756 devices per chip) were measured, not every device worked or had sufficient performance to consider in the analysis.

IV. SENSOR FIGURES OF MERIT

The goal of this section is first to introduce the different performance metrics that characterize RF-based IR sensors, including quality factor, fluctuation induced noise, responsivity, noise equivalent power, and time constant, and then to describe how they can be automatically measured using the proposed platform. In the following, performance metrics will illustrated using measured data from the RF-MEMS based IR sensors described in Section III.

A. QUALITY FACTOR

The quality factor is defined as the fractional bandwidth of the resonator, and is proportional to the ratio of energy stored by the resonator to the energy dissipated by the resonator in each cycle [42]. This metric is intrinsic to the performance of any resonant device. High quality devices exhibit a sharper resonance with higher quality factor. The home-made MATLAB software controls the VNA to automatically retrieve the admittance (Y) parameters of the device both in magnitude and phase. Using the measured data, the quality factor is extracted by finding the two points that are 3 dB below the maximum of the resonance peak. Fig. 10a shows the admittance response of an RF-MEMS IR sensor with and without IR illumination. Results clearly show the frequency shift of the resonant frequency and confirm that the device quality factor does not change upon radiation. Typical quality factors of the type of IR detectors measured here range from around $\sim$ 1000 to $\sim$ 2800.

B. FLUCTUATION INDUCED NOISE

The fluctuation induced noise represents the frequency instability of each resonator, is measured in Hz/$\sqrt{\text{Hz}}$, and can intuitively be understood as the variation of the resonator's resonance frequency versus time [43]. Thermal, mechanical, and RF noise sources are encountered in IR sensors which all contribute to their overall response [9]. To approximately quantify the fluctuation induced noise, an automated measurement process is implemented following the approach described in Ref. [9]. First, an algorithm finds the point of highest (negative) slope on the measured resonator admittance curve (see Fig. 10a) between the parallel and series resonances. Second, the VNA is set to operate in a continuous wave (CW) mode at exactly the high-slope frequency. In this operation mode, the VNA tracks the variations in amplitude and phase of the reflected signal versus time - an example of this result is shown in Fig. 10b. In the proposed system, a total of 16, 001 samples are acquired per device at a 10 KHz rate. Third, the data is processed to calculate the fluctuation induced noise [9]. Specifically, the root-means-square frequency noise is found as

$$f_n = \frac{\sigma_Y}{\frac{dY}{df}|_{f=f_o}\sqrt{\text{BW}}}, \tag{1}$$

where σ_Y represents the standard deviation of the CW admittance amplitude at the high slope point, BW represents the measurement bandwidth, and $\frac{dY}{df}|_{f=f_o}$ represents the slope of the admittance curve at the high slope point f_o. Here, the bandwidth refers to the intermediate frequency (IF) bandwidth of the VNA. The measured admittance fluctuations depend on the IF bandwidth used, therefore in order to normalize the admittance fluctuations it must be divided by the square root of the measurement bandwidth. The offset frequency is selected because we assume this point represents the largest frequency instability. This approximate approach has been employed in the literature to explore the noise response of RF-MEMS based IR sensors without requiring a signal source analyzer, yielding values of $\sim$ 1.46 Hz/$\sqrt{\text{Hz}}$ [9] and $\sim$ 1.0 Hz/$\sqrt{\text{Hz}}$ [10].

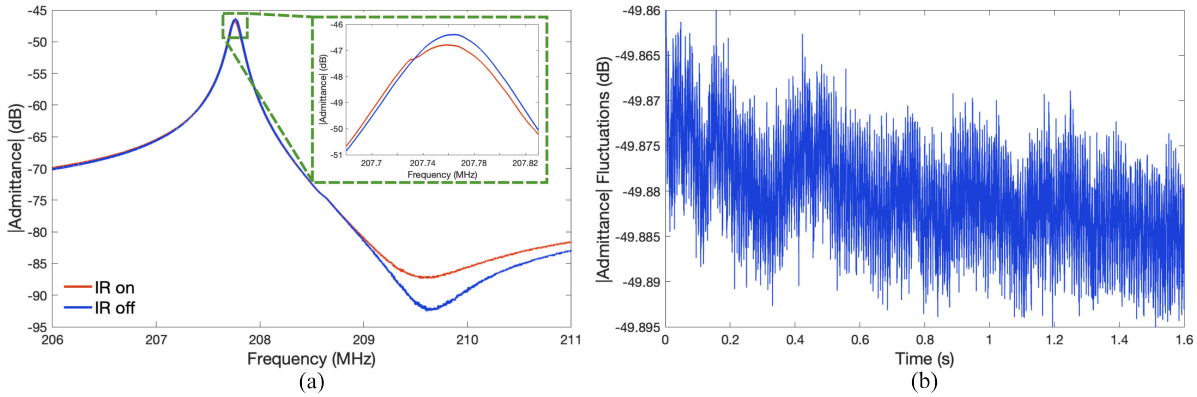

FIGURE 10. (a) The admittance of the device is plotted without IR (blue) and with IR (red) illumination. (b) The resonator is excited using a continuous RF wave at the high-slope point (207.8 MHz) and its admittance is measured over time.

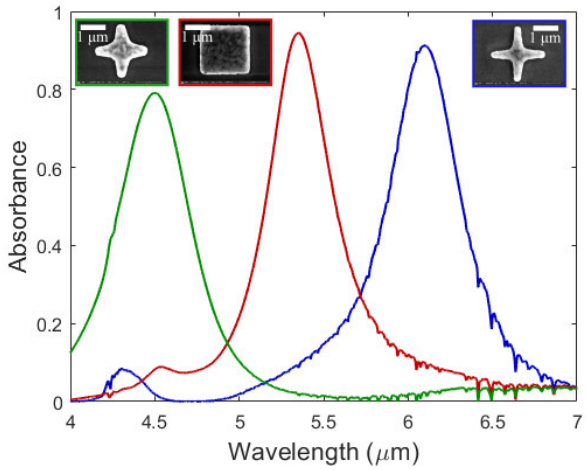

FIGURE 11. Measured IR spectra of various IR sensors. All devices share an identical CMR MEMS body but possess different ultrathin metasurfaces, and thus they are targeting different IR wavelengths. Insets show SEM images of the unit-cells that compose each of metasurfaces loading the devces.

C. RESPONSIVITY

The responsivity is related to the change of the sensor response upon incident IR radiation [1]. In case of the IR sensors described in Section III, the responsivity is calculated in Hz/W units as

$$R_V = \frac{\Delta f_s}{P_{IR}}, \tag{2}$$

where Δf_s is the resonance frequency shift caused by absorbed IR radiation (see Fig. 10a) and P_{IR} is the total IR power absorbed by the device in W. The resonance frequency shift depends on the thermal resistance of the device [9], which depends on the anchor geometry. Higher thermal resistances result in larger frequency shifts for the same incident power. Considering that the device is illuminated by broadband IR light, like the one coming from the blackbody radiator employed in the proposed system, the IR power absorbed by the device can be approximated by $P_{IR} = A \int E(\lambda)M(\lambda)d\lambda$, where A is the sensor area, $E(\lambda)$ is the blackbody spectral irradiance, and $M(\lambda)$ is the metasurface absorption profile. It should be stressed that the spectral absorption profile of the devices can be manipulated by adjusting the geometrical dimensions of the nanoresonators that compose the metasurfaces, as shown in Fig. 11 for some of the sensors described in Section III.

To calculate the IR power absorbed, the proposed platform requires to have pre-loaded the absorption spectra $M(\lambda)$ of the devices. In this study, this is performed beforehand using a Bruker Hyperiom 2000 Fourier-transform IR (FTIR) spectrometer. Additionally, the blackbody spectral irradiance is normalized using the in-band power measure on the stage (see Fig. 4). The resonance frequency shift Δf_s is experimentally obtained from the admittance of the device by measuring it with and without IR illumination. Other experimental studies of this type of IR sensors have reported responsivity values of $\sim$ 0.68 Hz/nW [9] and $\sim$ 0.53 Hz/nW [10]. It should be noted that this approach to measure responsivity is an approximation, as it (i) uses a broadband source, and thus cannot accurately retrieve the power absorbed at a specific wavelength; and (ii) neglects the potential influence of the out-of-band optical absorption in the device performance.

D. NOISE EQUIVALENT POWER

The NEP is one of the most important metrics in characterizing a sensor as it quantifies the sensitivity of the device [6].It is defined as the IR power that provide a signal to noise equal to 1 using a 1 Hz electrical bandwidth of the measurement [44], has units of $Hz/\sqrt{Hz}$, and it can be calculated as

$$NEP = \frac{f_n}{R_v}, \tag{3}$$

where f_n is the fluctuation induced noise $[Hz/\sqrt{Hz}]$ and R_v is the responsivity $[Hz/W]$. The NEP is obtained in the proposed platform by simply dividing the measured fluctuation induced noise by the responsivity. Previous NEP

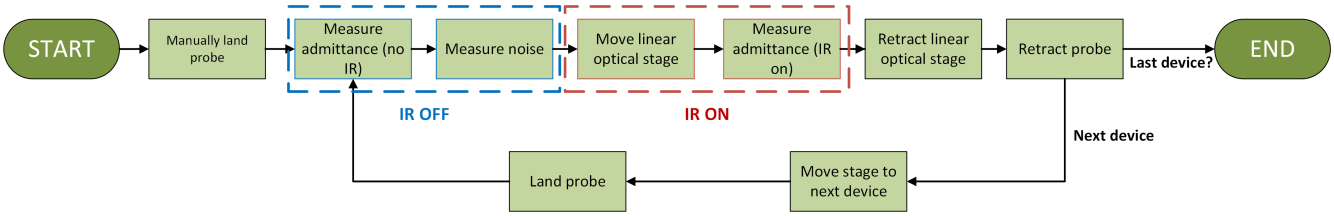

FIGURE 12. Diagram illustrating the automated system's control loop.

reported on RF MEMS-based IR sensors provide values of $\sim$ 1.9 nW/$\sqrt{\text{Hz}}$ [10] and $\sim$ 2.1 nW/$\sqrt{\text{Hz}}$ [9].

E. TIME CONSTANT

The time constant quantifies the speed in which a detector can respond to a stimulus. It can be defined as the time required to reach 63.2% of its full output from a step input. In the proposed platform, the time constant is measured by setting the VNA to CW mode, exciting the device at resonace, and monitoring the reflected signal versus time while chopping the incident IR light. The chopping frequency is increased until the admittance swing is 63.2% its full swing. The RF MEMS-based IR sensors measured here and elsewhere [8], [9], [10], [11] yield a time constant in the hundreds of μs.

V. SYSTEM OPERATION

This section describes how to operate the proposed platform to automatically characterize a large number of IR sensors located within the same chip. Before starting the automatized process, the following steps must be performed:

1) The platform software is updated with (i) the physical location of all devices within the chip; and (ii) the IR absorption profile of the metasurfaces.
2) The home-made vacuum chuck is leveled and adjusted.
3) The IR optics are well-aligned. This step can be verified using a IR detector card or a thermal image sensor.
4) The spatial power distribution of the blackbody radiation reaching the stage has been measured and loaded into the software.
5) The chip and calibration substrate are loaded onto the stage and aligned correctly onto the vacuum chuck.
6) The VNA is calibrated in the desired bandwidth. For the devices considered in Section III, a short-open-load procedure is employed using a CS5 calibration substrate [45].
7) The micro-probe is moved to the location where the IR light will illuminate the tip with maximum intensity. This measurement location will be employed to test all devices.
8) The stage hosting the chip is moved so the probe can be manually landed on the first device to be tested. This is performed using an external microscope (see Fig. 1).

Next, all devices within the chip can be automatically tested. Fig. 12 shows a system control loop diagram that illustrates the measurement algorithm. For each device, the following tasks are performed in sequential order: (i) measure the admittance parameters in the absence of IR light, as shown in Fig. 10a in blue line; (ii) determine the fluctuation induced noise as described in Section IV-B; and (iii) measure the admittance parameters illuminating the device with IR light, as shown in Fig. 10a in red line. In this last step, the linear stage is first moved into the optical path of the IR light and then retracted after the measurement is complete. It should be emphasized that measurements are only performed after the linear stage is stationary and data is never collected when any physical component of the system is moving. Once a device has been tested, the probe is retracted and then the stage is moved with micrometer precision to place the next device under test in the measurement location. The probe is automatically landed on the new device, and the process is repeated until all devices have been characterized. The testing rate of the system is $\sim$ 20 seconds per device.

The alignment procedure is of paramount importance to ensure proper probe landing on all devices. It is accomplished visually by moving the stage in a straight line across the chip and visually checking the movement of the microprobe relative to the devices in a column. If the microprobe does not follow the devices in a straight line, but instead deviates left or right, then an angular correction is applied to the chip by manually rotating the chip with the vacuum temporarily suspended. This process is repeated until the chip is properly aligned with the axes of the stage. When this happens, the XY translation stage will be able to accurately find any targeted device and properly control the micro-probe landing. Finally, it should be noted that the required angular tolerances depend on the device pad size and the overall chip size. For the chips tested in this work, a deviation of less than 0.5 degrees was necessary.

VI. RESULTS

This section summarizes the characterization of 1512 CMR MEMS IR sensors measured from two separate chips. A total of 756 from both the chip containing 1 μm thick CMR MEMS, and the chip containing 500 nm thick CMR MEMS. As stated in Section III, due to fabrication yield, not all devices worked or had sufficient performance to be included in the analysis. Therefore, the number of data points contained in some of the plots shown in this section may vary. A subset of the measurements characterizing the 1 μm devices was recently reported in Ref. [8],

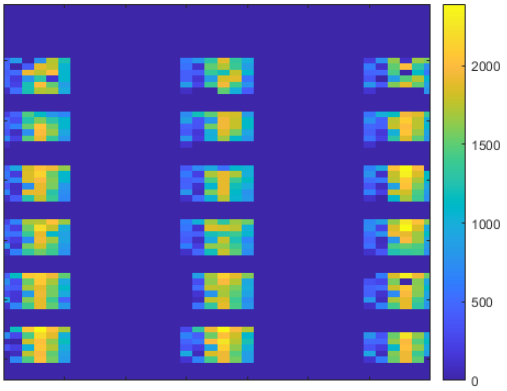

FIGURE 13. Spatial heat map of device performance is colored by resonator quality factor.

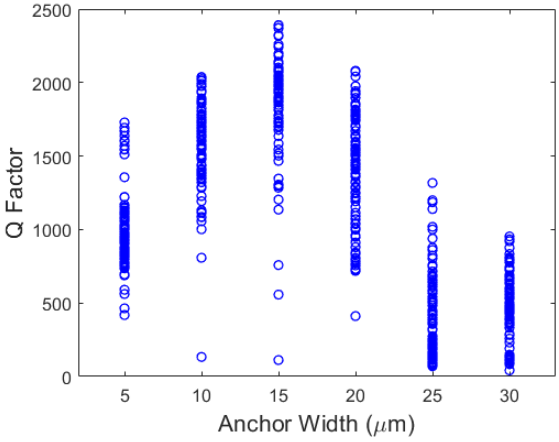

FIGURE 14. Measured quality factor of 1 μm thick CMR MEMS devices versus anchor width.

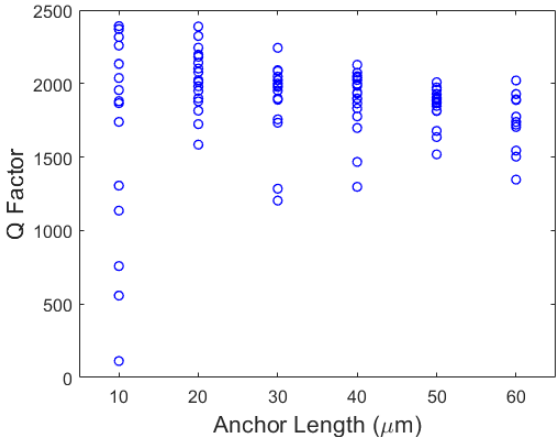

FIGURE 15. Measured quality factor of 1 μm thick CMR MEMS devices versus anchor length for anchors of width 15 μm.

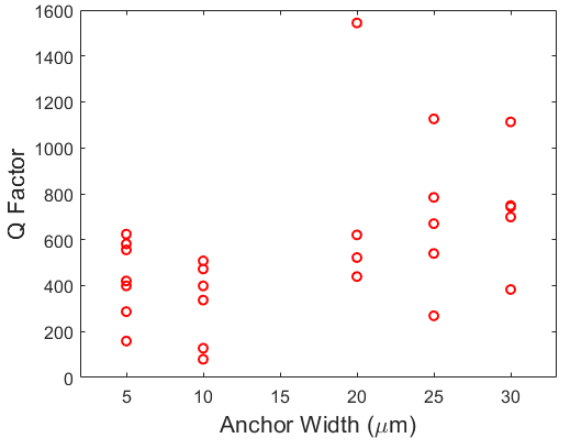

FIGURE 16. Measured quality factor of 500 *nm* thick CMR MEMS devices versus anchor width.

focusing on the underlying response and performance of RF MEMS-based IR sensors. Here, our study aims to compare the sensing performance of the devices versus the thickness of the piezoelectric material AlN and to devise optimal parameters. To this purpose, the proposed characterization platform is ideal: it can quickly record and calculate many useful device metrics, including quality factors, fluctuation induced noise, responsivity, and NEP, that can be correlated with design parameters, such as anchor and MEMS body dimensions and thickness, to better understand the sensors response and improve its design. Hundreds of thousands of datapoints in the form of admittance and time domain measurements have been collected. The processing of the data is automatically performed by the same software that controls the measurement platform.

Fig. 13 shows the spatial plot of device Q factor for all the CMR MEMS on the 1 μm chip. In the figure each pixel is a device whose color represents its quality factor. Like commercial wafer level test facilities, this platform generates spatial plots of different device parameters. Variation in Q between tiles, abnormally low Q or absence of Q entirely can be attributed to the fabrication yield mentioned in Section III. It should be noted the devices in the first row of tiles did not work, and therefore it seems there is only a 6×3 array of tiles. The variation between devices in a tile is due to the variation of anchor dimensions discussed in Section III, which controls the Q of the MEMS.

Fig. 14 shows the average Q factor versus anchor width for devices with AlN thickness of 1 μm. The average maximum Q occurs for an anchor width of 15 μm. Fig. 15 shows the average Q versus anchor length for devices with anchor width of 15 μm. Results confirm that the anchor's width plays a key role in the devices RF response whereas the influence of the anchor's lengths is moderate. Fig. 16 and Fig. 17 repeat these measurements for a CMR MEMS with AlN thickness of 500 nm. Optimal RF responses are found by devices with an anchor width and length of 20 and 40 μm, respectively. These results follow the trends and studies on anchor losses in CMR MEMS [46], [47] that do not operate as IR sensors.

Fig. 18 and Fig. 19 plot the responsivity versus thermal resistance (R_{Th}) for 1 μm thick and 500 nm thick CMR

TABLE 1. Statistics for CMR MEMS of different thicknesses.

	1 μm				500 nm			
	Average	Std	Median	Best	Average	Std	Median	Best
Q	1128	620	1092	2391	561	321	522	1544
Noise ($\frac{\text{Hz}}{\sqrt{\text{Hz}}}$)	0.548	0.286	0.449	0.257	0.911	0.498	0.740	0.440
Responsivity ($\frac{\text{Hz}}{\text{nW}}$)	15.4	9.35	11.6	73.3	36.4	39.3	24.6	164
NEP ($\frac{\text{pW}}{\sqrt{\text{Hz}}}$)	47.4	32.3	38.8	11.0	48.5	37.8	30.4	5.01

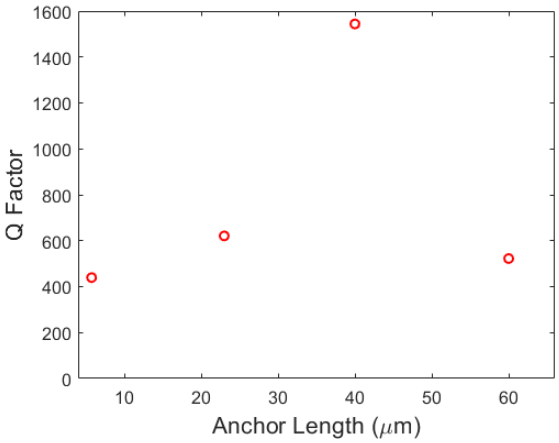

FIGURE 17. Measured quality factor of 500 *nm* thick CMR MEMS devices versus anchor length for anchors of width 20 μ*m*.

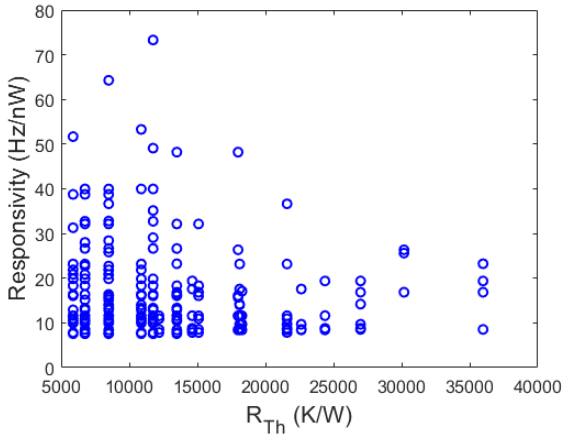

FIGURE 18. Responsivity versus thermal resistance for 1 μ*m* thick CMR MEMS IR sensors.

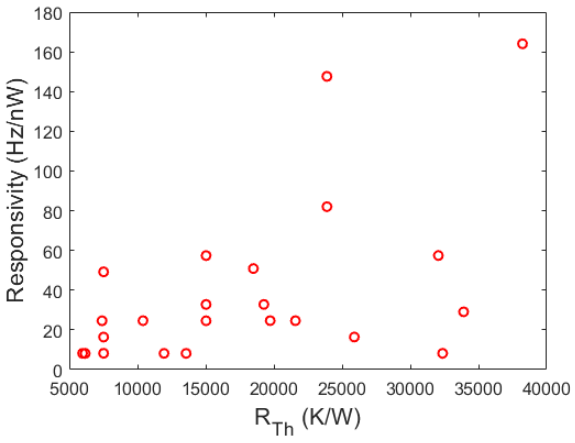

FIGURE 19. Responsivity versus thermal resistance for 500 *nm* thick CMR MEMS IR sensors.

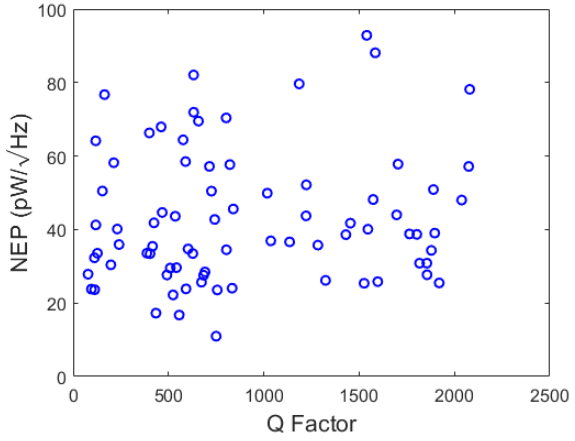

FIGURE 20. Noise equivalent power versus quality factor for 1 μ*m* thick CMR MEMS IR sensors.

MEMS respectively. The thermal resistance is theoretically approximated based on the device's anchor dimensions [9]. Additionally, Fig. 20 and Fig. 21 plot the NEP versus Q factor for 1 μ*m* thick and 500 nm thick CMR MEMS. As discussed in Section IV-D and also reported experimentally in other works [8], [9], [10], responsivity and NEP are closely related. However, devices with the highest RF quality factor may not simultaneously exhibit the largest responsivity, and thus they may not become highly-performing IR sensors. Therefore, it is possible for devices with lower Q to also have a low NEP and high responsivity. Our study demonstrates the ability of the proposed platform to characterize and study a large variety of device metrics to determine potential trends and optimal responses.

Table 1 overviews the quality factor, fluctuation induced noise, responsivity, and NEP for CMR MEMS with AlN thicknesses of 1 μ*m* and 500 *nm*. The average and best Q for the 1 μ*m* thick CMR MEMS are 1128 and 2391 respectively, with specific values depending on the anchor dimensions as shown in Figs. 14 and 15. The average and best quality factor for the 500 *nm* thick CMR MEMS were smaller, with values of 561 and 1544, respectively. Similar trends are observed in the noise response. The average and best

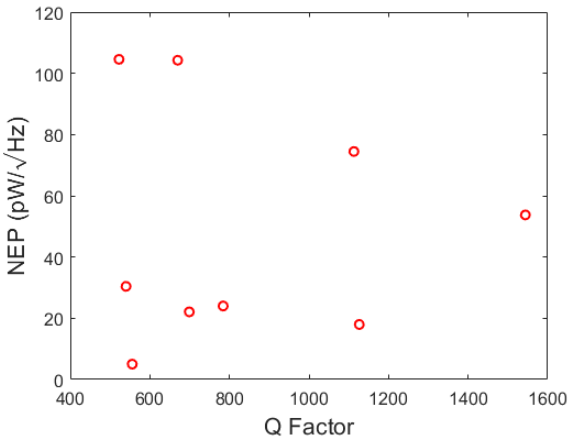

FIGURE 21. Noise equivalent power versus quality factor for 500 *nm* thick CMR MEMS IR sensors.

fluctuation induced noise for devices with 1 μm thick AlN were 0.548 $\sqrt{\text{Hz}}$ and 0.257 $\sqrt{\text{Hz}}$ respectively, values that increase by almost a factor of 2 in the case of 500 *nm* thick devices. This response means thinner devices should be more affected by all noise contributions, including mechanical and thermal. In both cases, the best noise performance was found in devices with high quality factor - as expected from other studies [8]. It should also be noted that these measured data constitutes a significant improvement with respect to previous noise metrics reported in the literature, which include values of 1.46 Hz/$\sqrt{\text{Hz}}$ in Ref. [9] and 1.0 Hz/$\sqrt{\text{Hz}}$ in Ref. [10]. A highest responsivity of 164 Hz/nW was found in a 500 *nm* thick device, whereas the average responsivity for sensors with this thickness is 36.4 Hz/nW. These values are approximate double to the ones found in devices with 1 μm thick AlN. As a result, the lowest NEP measured for the thicker devices was 11.0 pW/$\sqrt{\text{Hz}}$, a value that slightly decreases down to 5.01 pW/$\sqrt{\text{Hz}}$ for the thinner ones. These metrics provides the most important conclusion of our experimental study: thinner RF-MEMS based IR sensors exhibit both a larger responsivity and larger fluctuation induced noise that thicker structures, and the combination of these two contributions leads roughly similar NEP that the one found in thicker devices. As a result, it might be more convenient to operate with thicker structures −in this case, RF MEMS based on as 1 μm thick AlN− as they are usually easier to fabricate and more resilient to environmental variations.

The performance of the reported sensors makes them very well suited for a wide range of applications, with emphasis in those in which IR spectral selectivity is required. Examples include the accurate detection of specific gases [48], molecules [49], or oncometabolites (useful for cancer diagnosis) [50], [51], [52] that exhibit specific spectral fingerprints in the IR region. Moving beyond, this technology has the potential to be integrated with CMOS platforms to develop on-chip IR spectroscopy systems with significant applications in many areas, including healthcare, sensing, physics, and biology.

VII. CONCLUSION

This paper has presented an automated platform for the characterization of on-chip IR sensors, quickly gathering metrics such as RF quality factor, fluctuation induced noise, responsivity, and noise equivalent power. The system is composed of a high precision 2D stage, a micro-probe equipped with a stepper motor for automatic landing, a VNA, a blackbody radiators, and an IR optics assembly on a linear stage. These components are controlled using a Teensy microcontroller that interfaces with stepper motors and a software running a tailored automatized algorithm. The system is designed to characterize thousands of devices within a single chip, taking an average of around $\sim$ 20 seconds per sensor. To demonstrate the system performance in practice, 1512 RF CMR MEMS based IR sensors with different thickness have been characterized. Results experimentally confirm that thicker (1 μm AlN) devices exhibit lower responsivity and noise that thinner devices (500 nm AlN). Our experimental study shows that the behavior of these two mechanisms with respect to device thickness is opposite and tend to balance, thus leading to roughly similar NEP in the $\sim$ 20 pW/$\sqrt{\text{Hz}}$ range. The proposed platform is able harvest vast amount of data and to quickly generate statistics of measured metrics versus the geometrical dimensions of the sensors under test. Additionally, the system is flexible and can easily incorporate different IR sources, such as optical parametric oscillators [23], and dedicated instrumentation to measure phase noise [53], to enhance its capabilities. Further improvements can be made by using an XYZ stage as the sample stage, which eliminates the need for motorized control of the micro-probe arm since the z-axis can be used in its place, or by using a motorized shutter for the IR light that removes the need of a linear stage.

REFERENCES

[1] R. G. Driggers, M. H. Friedman, and J. Nichols, *Introduction To Infrared and Electro-Optical Systems*. Norwood, MA, USA: Artech House, 2012.

[2] G. H. Rieke, "Infrared detector arrays for astronomy," *Annu. Rev. Astron. Astrophys.*, vol. 45, no. 1, pp. 77–115, Sep. 2007, doi: 10.1146/annurev.astro.44.051905.092436.

[3] A. Kendel and B. Zimmermann, "Chemical analysis of pollen by FT-Raman and FTIR spectroscopies," *Frontiers Plant Sci.*, vol. 11, p. 352, Mar. 2020.

[4] P. Mohamed Shakeel, T. E. El. Tobely, H. Al-Feel, G. Manogaran, and S. Baskar, "Neural network based brain tumor detection using wireless infrared imaging sensor," *IEEE Access*, vol. 7, pp. 5577–5588, 2019, doi: 10.1109/ACCESS.2018.2883957.

[5] K.-Y. Su and W.-L. Lee, "Fourier transform infrared spectroscopy as a cancer screening and diagnostic tool: A review and prospects," *Cancers*, vol. 12, no. 1, p. 115, Jan. 2020.

[6] A. Rogalski, *Infrared Detectors*, 2nd ed., Boca Raton, FL, USA: CRC Press, 2010, pp. 33–40.

[7] S. Huang, H. Tao, I.-K. Lin, and X. Zhang, "Double-cantilever infrared detector: Fabrication, curvature control and demonstration of thermal detection," in *Proc. Int. Solid-State Sensors, Actuat. Microsystems Conf.*, Lyon, France, 2007, pp. 1601–1604, doi: 10.1109/sensor.2007.4300454.

[8] M. E. Gülseren, M. Benson, R. W. Parker, J. Segovia-Fernandez, E. T.-T. Yen, and J. S. Gómez-Díaz, "Experimental study of spectrally selective MEMS/metasurface infrared detectors," *IEEE Sensors J.*, vol. 24, no. 11, pp. 17313–17323, Jun. 2024, doi: 10.1109/JSEN.2024.3388966.

[9] Y. Hui, J. S. Gomez-Diaz, Z. Qian, A. Alù, and M. Rinaldi, "Plasmonic piezoelectric nanomechanical resonator for spectrally selective infrared sensing," *Nature Commun.*, vol. 7, no. 1, p. 11249, Apr. 2016.
[10] Y. Hui, S. Kang, Z. Qian, and M. Rinaldi, "Uncooled infrared detector based on an aluminum nitride piezoelectric fishnet metasurface," *J. Microelectromech. Syst.*, vol. 30, no. 1, pp. 165–172, Feb. 2021.
[11] J. Tao, Z. Liang, G. Zeng, D. Meng, D. R. Smith, Q. H. Liu, Q. Yang, M. Zhang, W. Pang, J. Liang, and T. Bourouina, "Dual functionality metamaterial enables ultra-compact, highly sensitive uncooled infrared sensor," *Nanophotonics*, vol. 10, no. 4, pp. 1337–1346, Feb. 2021.
[12] S. J. Pi. *Conquering the Silicon Photonics Production Bottleneck*. Accessed: Sep. 13, 2024. [Online]. Available: https://www.photonics.com
[13] Scott Jordan. *Automating Photonic Alignment Addresses Silicon Photonics Production Bottleneck*. Accessed: Sep. 13, 2024. [Online]. Available: www.us-tech.com
[14] P. Zhang, B. Tang, Y. Yang, B. Li, R. Liu, L. Xie, Z. Li, and F. Lin, "Test system for wafer-level silicon-photonics testing," *Proc. SPIE*, vol. 11548, pp. 294–301, Oct. 2020, doi: 10.1117/12.2573456.
[15] J. G. F. Flores, C. Nasseraddin, J. Solomon, T. Yerebakan, A. B. Matsko, and C. W. Wong, "AtOMICS: A neural network-based automated optomechanical intelligent coupling system for testing and characterization of silicon photonics chiplets," 2022, *arXiv:2210.16946*.
[16] A. Aboketaf, C. Hedges, V. Dhurgude, B. Harris, F. Guan, F. Pavlik, T. Anderson, A. Stricker, Y. Bian, M. Rakowski, and A. Dasgupta, "Towards fully automated testing and characterization for photonic compact modeling on 300-mm wafer platform," in *Proc. Optical Fiber Commun. Conf.*, Jan. 2021, pp. 1–6, doi: 10.1364/ofc.2021.w6a.1.
[17] S. Gießmann and F.-M. Werner, "Wafer level test solutions for IR sensors," *Proc. SPIE*, vol. 9071, May 2014, Art. no. 907111, doi: 10.1117/12.2053852.
[18] R. Zhang and F. G. Shi, "Manufacturing of laser diode modules: Integration and automation of laser diode-fiber alignment and RIN characterization," *IEEE Trans. Adv. Packag.*, vol. 26, no. 2, pp. 128–132, May 2003, doi: 10.1109/TADVP.2003.817473.
[19] C. Gong and D. Mehrl, "Characterization of the digital micromirror devices," *IEEE Trans. Electron Devices*, vol. 61, no. 12, pp. 4210–4215, Dec. 2014, doi: 10.1109/TED.2014.2361855.
[20] R. W. Whatmore, "Pyroelectric devices and materials," *Rep. Prog. Phys.*, vol. 49, no. 12, pp. 1335–1386, Dec. 1986.
[21] P. L. Richards, "Bolometers for infrared and millimeter waves," *J. Appl. Phys.*, vol. 76, no. 1, pp. 1–24, Jul. 1994.
[22] B. Abdullah Aloyaydi, S. Sivasankaran, and H. Rizk Ammar, "Influence of infill density on microstructure and flexural behavior of 3D printed PLA thermoplastic parts processed by fusion deposition modeling," *AIMS Mater. Sci.*, vol. 6, no. 6, pp. 1033–1048, 2019.
[23] S. E. Harris, "Tunable optical parametric oscillators," *Proc. IEEE*, vol. 57, no. 12, pp. 2096–2113, Dec. 1969, doi: 10.1109/proc.1969.7495.
[24] J. Faist, F. Capasso, D. L. Sivco, C. Sirtori, A. L. Hutchinson, and A. Y. Cho, "Quantum cascade laser," *Science*, vol. 264, no. 5158, pp. 553–556, Apr. 1994.
[25] *RCN Series—High Temperature Cavity Blackbody*. HGH Infrared USA. Accessed: Sep. 13, 2024. [Online]. Available: https://hgh-infrared-usa.com/rcn-series/
[26] *Thorlabs—PDAVJ10 HgCdTe Amplified Photodetector, 2.0–10.6 µm, DC-100 MHz BW, 1 mm², 100–120 or 220–240 VAC*. Accessed: Sep. 13, 2024. [Online]. Available: https://www.thorlabs.com/thorproduct.cfm?partnumber=PDAVJ10
[27] *MLFI 500 KHz/5 MHz Lock-in Amplifier*. Zurich Instruments. Accessed: Sep. 13, 2024. [Online]. Available: https://www.zhinst.com/americas/en/products/mfli-lock-in-amplifier
[28] *Barium Fluoride (BaF2) Lenses*. EKSMA Optics. Accessed: Sep. 13, 2024. [Online]. Available: https://eksmaoptics.com/optical-components/uv-and-ir-optics/barium-fluoride-baf2-lenses/
[29] *PF10-03-M02-Ø1, 'Mid-Infrared Enhanced Gold Mirror' Thorlabs*. Accessed: Sep. 13, 2024. [Online]. Available: https://www.thorlabs.com/thorproduct.cfm?partnumber=PF10-03-M02
[30] *GGB Industries | Model 40A*. Accessed: Sep. 13, 2024. [Online]. Available: https://ggb.com/home/model-40a/
[31] S. Reifel. *Stan-Reifel/Speedystepper: Stepper Motor Control Library for Arduino*. GitHub. Accessed: Sep. 13, 2024. [Online]. Available: https://github.com/Stan-Reifel/SpeedyStepper
[32] P. Stoffregen. *Teensy 4.0*. Accessed: Sep. 13, 2024. [Online]. Available: https://www.pjrc.com/store/teensy40.html
[33] Arduino. (2022). *UNO R3 | Arduino Documentation*. [Online]. Available: https://docs.arduino.cc/hardware/uno-rev3
[34] (2013). *DRV8825*. [Online]. Available: www.ti.com/product/DRV8825
[35] *TR1300/1 2-Port 1.3 GHz Analyzer*. Copper Mountain Technologies. Accessed: Sep. 13, 2024. [Online]. Available: https://coppermountaintech.com/vna/tr1300-1-2-port-1-3-ghz-analyzer/
[36] T. Badloe, J. Mun, and J. Rho, "Metasurfaces-based absorption and reflection control: Perfect absorbers and reflectors," *J. Nanomaterials*, vol. 2017, pp. 1–18, Jan. 2017.
[37] C. Wu, N. Arju, G. Kelp, J. A. Fan, J. Dominguez, E. Gonzales, E. Tutuc, I. Brener, and G. Shvets, "Spectrally selective chiral silicon metasurfaces based on infrared Fano resonances," *Nature Commun.*, vol. 5, no. 1, p. 3892, May 2014.
[38] M. Zhang, J. Fang, F. Zhang, J. Chen, and H. Yu, "Ultra-narrow band perfect absorbers based on Fano resonance in MIM metamaterials," *Opt. Commun.*, vol. 405, pp. 216–221, Dec. 2017.
[39] M. F. Limonov, M. V. Rybin, A. N. Poddubny, and Y. S. Kivshar, "Fano resonances in photonics," *Nature Photon.*, vol. 11, no. 9, pp. 543–554, Sep. 2017.
[40] Z. Liu, L. Guo, and Q. Zhang, "A simple and efficient method for designing broadband terahertz absorber based on singular graphene metasurface," *Nanomaterials*, vol. 9, no. 10, p. 1351, Sep. 2019.
[41] S. Kang, Z. Qian, V. Rajaram, S. D. Calisgan, A. Alù, and M. Rinaldi, "Ultra-narrowband metamaterial absorbers for high spectral resolution infrared spectroscopy," *Adv. Opt. Mater.*, vol. 7, no. 2, Nov. 2018, Art. no. 1801236.
[42] D. M. Pozar, *Microwave Engineering*. Hoboken, NJ, USA: Wiley, 2011.
[43] A. N. Cleland and M. L. Roukes, "Noise processes in nanomechanical resonators," *J. Appl. Phys.*, vol. 92, no. 5, pp. 2758–2769, Sep. 2002.
[44] S. Leclercq, "Discussion about noise equivalent power and its use for photon noise calculation," Rep. FOV Opt. Bolometer Projects 30m Telescope, Int. Res. Inst. Radio Astron. (IRAM), France, Tech. Rep. 1, 2007.
[45] *GGB Industries | Calibration Substrate*. Accessed: Sep. 13, 2024. [Online]. Available: https://ggb.com/home/calibration-substrate/
[46] J. Segovia-Fernandez, M. Cremonesi, C. Cassella, A. Frangi, and G. Piazza, "Experimental study on the impact of anchor losses on the quality factor of contour mode AlN resonators," in *Proc. Transducers Eurosensors, 17th Int. Conf. Solid-State Sensors, Actuat. Microsystems*, Barcelona, Spain, Jun. 2013, pp. 2473–2476, doi: 10.1109/Transducers.2013.6627307.
[47] J. Segovia-Fernandez, M. Cremonesi, C. Cassella, A. Frangi, and G. Piazza, "Anchor losses in AlN contour mode resonators," *J. Microelectromech. Syst.*, vol. 24, no. 2, pp. 265–275, Apr. 2015, doi: 10.1109/JMEMS.2014.2367418.
[48] D. Popa and F. Udrea, "Towards integrated mid-infrared gas sensors," *Sensors*, vol. 19, no. 9, p. 2076, May 2019.
[49] R. Eischens and W. Pliskin, "The infrared spectra of adsorbed molecules," in *Advances in Catalysis*, vol. 10. Amsterdam, The Netherlands: Elsevier, 1958, pp. 1–56.
[50] A. Zlotogorski-Hurvitz, B. Z. Dekel, D. Malonek, R. Yahalom, and M. Vered, "FTIR-based spectrum of salivary exosomes coupled with computational-aided discriminating analysis in the diagnosis of oral cancer," *J. Cancer Res. Clin. Oncol.*, vol. 145, no. 3, pp. 685–694, Mar. 2019.
[51] J. Backhaus, R. Mueller, N. Formanski, N. Szlama, H.-G. Meerpohl, M. Eidt, and P. Bugert, "Diagnosis of breast cancer with infrared spectroscopy from serum samples," *Vibrational Spectrosc.*, vol. 52, no. 2, pp. 173–177, Mar. 2010.
[52] N. Brasier and J. Eckstein, "Sweat as a source of next-generation digital biomarkers," *Digit. Biomarkers*, vol. 3, no. 3, pp. 155–165, Dec. 2019.
[53] *E5052B Signal Source Analyzer (SSA)*. Keysight. Accessed: Sep. 13, 2024. [Online]. Available: https://www.keysight.com/us/en/product/E5052B/signal-source-analyzer-ssa.html

MATTHEW BENSON was born in Los Angeles, CA, USA. He received the B.S. degree in electrical engineering from the University of California at Davis, CA, USA, in 2021, where he is currently pursuing the Ph.D. degree in electrical engineering.

His research interests include the areas of infrared and terahertz sensing, MEMS/NEMS devices, and metamaterials.

RYAN W. PARKER was born in San Diego, CA, USA, in 1997. He received the B.S. and M.S. degrees in electrical engineering from the University of California at Davis, CA, USA, in 2023.

From 2021 to 2023, he was a Student Researcher with the Applied Micro/Nano Electromagnetics Research Laboratory. Since 2023, he was been a Product Design Engineer with Texas Instruments Inc. (RFAB), Dallas, TX, USA.

MELISA EKIN GÜLSEREN (Member, IEEE) received the B.S. and M.S. degrees in electrical and electronics engineering from Bilkent University, Ankara, Türkiye, in 2016 and 2019, respectively. She is currently pursuing the Ph.D. degree in electrical and computer engineering with the University of California at Davis, CA, USA.

Her research interests include MEMS/NEMS devices, metamaterials, and micro-/nano-fabrication.

JUAN SEBASTIÁN GÓMEZ-DÍAZ (Senior Member, IEEE) received the M.S. and Ph.D. degrees in electrical engineering from the Technical University of Cartagena, Cartagena, Spain, in 2006 and 2011, respectively.

He is currently a Professor with the Electrical and Computer Engineering Department, University of California at Davis, Davis, CA, USA. During the development of the Ph.D. degree, he held visiting research positions with the École Polytechnique de Montréal, Montreal, QC, Canada, and the Fraunhofer Institute for High Frequency Physics and Radar Techniques, Wachtberg, Germany. From 2011 to 2014, he was a Postdoctoral Fellow with the École Polytechnique Fédérale de Lausanne (EPFL), Lausanne, Switzerland. From 2014 to 2016, he continued his postdoctoral work with the Metamaterials and Plasmonic Research Laboratory, The University of Texas at Austin, Austin, TX, USA. His main research interests include applied electromagnetics, plasmonics, 2-D materials, metasurfaces, nonreciprocal and hyperbolic responses, MEMS, and other emerging topics in nanotechnology. As a PI, his research work has been funded by the National Science Foundation, the National Institutes of Health, the U.S. Department of Defense, the Semiconductor Research Corporation, and the Keck Foundation, among other funding agencies.

Dr. Gómez-Díaz is also a UC Davis Chancellor Fellow (class of 2023). He received the 2023 UC Davis Graduate Program Advising and Mentoring Award, the 2018 NSF CAREER Award, the 2017 Leopold Felsen Award for Excellence in Electrodynamics, the Raj Mittra Award presented by the 2015 IEEE Antennas and Propagation Society, the Young Scientist Award of the 2015 URSI Atlantic Radio Science Conference, a FP7 Marie Curie Postdoctoral Fellowship from the European Commission in 2012, and the Colegio Oficial de Ingenieros de Telecomunicación (COIT/AEIT) Award to the best Spanish Ph.D. thesis in information and communication technologies. He serves as a reviewer for many journals in the fields of engineering and physics.